Aqueous inks for ecofriendly processing of organic solar cells: Investigation of morphological changes

Maxime M Rammal, Paul Nizet, Géraldine Layrac, Sufal Swaraj, Benoît Heinrich, Jiang Jing, Emilie Steveler, Thomas Heiser, Nicolas Leclerc, Patrick Lévêque, et al.

Aqueous inks for ecofriendly processing of organic solar cells: investigation of morphological changes

Maxime M. Rammal,[a] Paul Nizet,[ab] Géraldine Layrac,[a] Sufal Swaraj,[c] Benoît Heinrich,[d] Jiang Jing,[b] Émilie Steveler,[b] Thomas Heiser,[b] Nicolas Leclerc,[a] Patrick Lévêque,*[b] and Anne Hébraud*[a]

[a] Institut de Chimie et Procédés pour l'Énergie, l'Environnement et la Santé (ICPEES), Université de Strasbourg - CNRS, UMR 7515, École Européenne de Chimie, Polymères et Matériaux (ECPM), 25 Rue Becquerel, 67087 Strasbourg Cedex 02, France. *E-mail : anne.hebraud@unistra.fr
[b] Laboratoire ICube, UMR 7357-CNRS, Université de Strasbourg, 23 rue du Loess, 67037 Strasbourg, France. *E-mail: patrick.leveque@unistra.fr
[c] Synchrotron SOLEIL, L'Orme des Merisiers, Saint-Aubin, BP 48, 91192 Gif-sur-Yvette Cedex, France.
[d] Université de Strasbourg, CNRS, IPCMS UMR 7504, F-67034 Strasbourg, France.

Abstract

Aqueous dispersions of organic semiconducting nanoparticles (NPs) are particularly attractive as inks for the environmentally friendly preparation of organic solar cells. The internal morphology of the NPs, which depends on their elaboration process, is a key parameter, which has a significant influence on the final morphology of the active layer and therefore its effectiveness. In the present study, core-shell (PF2:$PC_{71}BM$) NPs were prepared by miniemulsion. Their internal morphology including the composition of the two phases was characterized by scanning transmission X-ray microscopy (STXM) showing a core composed of 77% $PC_{71}BM$ and a shell composed of 75% PF2. It was found that thermal annealing promotes $PC_{71}BM$ diffusion from the core to the shell, increasing its proportion in the shell from 25% to 42%. This annealing, when applied after NPs deposition by spincoating, allows partial coalescence of the NPs, reducing the roughness of the active layer, and increases electron mobility, thus demonstrating the formation of $PC_{71}BM$ percolation paths for electron transport. A PCE of 1.6% could thus be obtained after 10 min of thermal annealing at 100°C. At higher temperature, Grazing-Incidence Wide-Angle X-Ray Scattering (GIWAXS) analyses demonstrate the modification of the PF2 structuration from randomly oriented lamella after deposition to edge-on orientation after annealing, leading to an unfavorable decrease of the hole mobility in the direction perpendicular to the substrate, while increasing the hole mobility in the substrate plane. This study demonstrates the need to systematically characterize the internal morphology of NPs in order to rationalize the morphology of the active layer and optimize its properties.

Introduction

Global warming due to excess CO_2 in the atmosphere renders the need to replace fossil fuels with renewable energies ever more pressing. In this context, organic photovoltaic modules are particularly interesting as they are much lighter than their silicon-based counterparts, flexible, semi-transparent and require less energy to produce. In recent years, major efforts to design new organic semiconducting (OSC) materials have resulted in a steady increase in efficiencies reaching more than 19% for single junction devices.[1,2] However, these polymers are highly crystalline with a very low processability in organic solvent. Therefore, they have to be deposited, sometimes at high temperature, from halogenated solvents, whose toxicity makes their large-scale manufacturing process incompatible with health and environmental safety standards. As the morphology of the active layer, composed of donor (D) and acceptor (A) materials is a key factor in the performance of photovoltaic cells, and is highly dependent on the casting stage, the eco-compatible implementation of these new molecules, without loss of efficiency, is not easy. Two approaches are currently being studied: the search for alternative, non-toxic solvents[3,4] and the use of dispersions of organic semiconducting nanoparticles (NPs), also called inks, in non-toxic solvents such as water or ethanol.[5] The use of aqueous inks is a common approach in industrial processes, as it avoids the user being in contact with potentially toxic organic solvents. Therefore, the development and study of organic semiconducting NPs is a necessary

step that could help the industrial development of organic photovoltaics. For OPV application, the nanoparticles must contain the D and A materials, and their assembly in the solid state must form the required D/A heterojunction distributed in volume with suitable material morphologies, which is not easy to control.

The organic semiconducting NPs can be prepared by miniemulsion or nanoprecipitation. In the miniemulsion technique, the OSC materials are first solubilized in a solvent that is not miscible with water, and necessitate the presence of a surfactant in order to prepare a miniemulsion of the organic phase in water, prior to the evaporation of the solvent. The final morphology of the NP depends on the evaporation kinetics,[6] the interaction of the D and A materials with the surfactant[7] and their surface tension,[8,9] often leading to a core-shell morphology with the material having the higher surface tension in the core of the NP. The nanoprecipitation is less versatile as the polymers have to be soluble in a more polar solvent, miscible with water, such as THF and due to its mechanism, often produces very dilute NP dispersions.[10,11] However, its fast kinetics usually leads to intermixed bulk heterojunction (BHJ) NPs,[12] an ideal morphology for the final active layer.

Recently, we investigated a fluorinated electron donor low bandgap polymer, called PF2. This polymer is composed of a difluorinated benzo[2,1,3]thiadiazole electron deficient unit sandwiched between two thiophene units bearing long and ramified alkyl side-chains and a fused thieno[3,2-*b*]thiophene ring (**Fig. 1a**). Thanks to the long and ramified side-chains and to the fluorine atoms, this PF2 polymer exhibits a favorable face-to-face lamellas orientation and high stacking cohesion and domain purities, leading to high power conversion efficiencies (PCEs) in binary[13] and ternary[14] solar cells even on very large active areas (over 66 cm^2).[15] However, this increased stacking cohesion also results in a poor solubility in most solvents. Consequently, PF2, as many of fluorinated conjugated polymers, needs to be processed at high temperature in organic solvents to control its aggregation during cooling. Therefore, herein, we developed the NP approach for the (PF2:$PC_{71}BM$) blend. Because of the very low PF2 solubility, NPs were prepared by miniemulsion. In this work, in addition to the NP synthesis methodology development, we investigated the NP's internal morphology by Transmission Electron Microscopy (TEM) and Scanning Transmission X-ray Microscopy (STXM) and prepared the active layer thin films. Finally, the parallel and perpendicular charge carrier mobilities and the solar cell power conversion efficiency were measured as a function of the thin-film annealing temperature and related to the structuration of the materials as observed by GIWAXS.

Experimental part

Materials:

PF2 was synthesized as described in Ibraikulov *et al.*[13] The batch synthesized for this work exhibits a high molar mass value in number of 44 kg/mol, and a polydispersity index Đ=1.8, as measured by Size

Exclusion Chromatography in trichlorobenzene (detailed measurement procedure and chromatogram can be found in the ESI, **Fig. S1**). $PC_{71}BM$ was purchased from Ossila. Sodium dodecylsulfate (SDS) and all other reagents and chemicals were purchased from Aldrich or TCI.

Nanoparticles preparation

The NPs were prepared using a miniemulsion evaporation method. PF2 and PCBM solutions at 1 $mg.mL^{-1}$ in $CHCl_3$ were prepared and heated at 60°C for 24 hours prior to their use. A total of 1mL organic phase (precise amount of each solution depending on the D:A ratio) was added into 1.75 mL of an SDS aqueous solution at 4 $mg.mL^{-1}$ followed by agitation for 1 hour at 500 rpm to obtain a coarse macroemulsion. Miniemulsion was then formed after sonication for 3 min at an amplitude of 40% (Branson Sonifier 400 W). The miniemulsion was then heated at 60°C in a sand bath for around 180 min, under magnetic stirring at 500 rpm, to insure a complete $CHCl_3$ evaporation. During the evaporation, the flask was covered by anti-dust paper.

Dynamic light scattering DLS: The size and distribution measurements of NPs were performed with a CGS-3 goniometer (ALV) equipped with a monochromatic helium-neon laser with a wavelength of 633 nm. The diluted suspension having a concentration of 0.001 to 0.002 $mg.mL^{-1}$ was placed in 10 × 75 mm glass tubes in a thermostated toluene bath (20°C). An angle $\theta = 90°$ was imposed between the incident beam and the detector.

Fluorescence spectroscopy: Florescence spectroscopy analyses were performed with a FluoroMax-4 spectrometer (Horiba Scientific) in 10 mm wide quartz cells. A suspension concentration of approximately 0.002 $mg.mL^{-1}$ was needed. The optical blank was performed with a quartz cell containing pure water-MQ. Fluorescence spectra were obtained by selecting an excitation wavelength of 630 nm and scanning the emission wavelengths from 650 to 800 nm.

Photoluminescence PL spectroscopy: The samples of 0.1 $mg.mL^{-1}$ were excited using 90 ps light pulses of 0.05 nJ energy at 515 nm and 20 MHz repetition rate from a Spectra-Physics Mai Tai laser. Time resolved-PL was measured using a Hamamatsu C6860 streak camera with a S-20 photocathode in synchro scan mode. The instrument response function (IRF) of the setup was 10 ps at full width half maximum (FWHM). Laser pulse duration being much greater than the response time of the system, the temporal resolution is of the order of a hundred ps.

Scanning electron microscopy SEM: Morphological aspects of NPs were analyzed by SEM (Vega 3 TESCAN) in high vacuum mode with a voltage of 5 kV. Few drops of the dialysed NPs suspension were drop casted on aluminum paper. After water evaporation for 18 hours, they were then coated by a thin layer of gold with a sputter coater (Q150RS, Quorum).

Transmission Electron Microscopy TEM: Morphological and structural aspects of NPs were analyzed by Dris Ihiawakrim on the IPCMS electron microscopy platform using JEOL 2100 F LaB6 200Kv with a resolution of 0.21 nm, equipped with a STEM detector. Samples of NPs

suspension with a concentration of 0.57 mg.mL^{-1} were deposited on copper TEM grids and dried at room temperature for a few hours.

Scanning Transmission X-ray Microscopy STXM: Scanning Transmission X-ray Microscopy was performed at the STXM instrument (RI GmbH) at HERMES[16] beamline at synchrotron SOLEIL. A zone plate of 25 nm outer zone width was used (Applied Nanotools Inc., Canada) to focus the horizontally polarized monochromatic x-rays on the sample. A photomultiplier tube (PMT) capped with a phosphorus screen was used to detect the transmitted photons. Beamline energy calibration was performed by measuring the 3p Rydberg peak of CO_2 gas, finding the difference from the literature reference value of 294.96 eV,[17] and applying this difference to all spectral energy values. Thin films (200-300 nm) of PF2 and $PC_{71}BM$ were prepared and floated onto TEM grids for measurement of NEXAFS (Near edge x-ray absorption fine structure) of the pure materials. The X-rays were incident normal to the sample surface. Energy stacks were obtained at the Carbon K-edge for all the samples. Diluted dialysed NPs suspensions were then drop-casted onto silicon nitride membrane windows (Norcada Inc.) for STXM measurements. The STXM analysis software aXis2000 (ref: aXis2000 source http://unicorn.mcmaster.ca/aXis2000.html), was used for the singular value decomposition (SVD) of the NPs stacks using the NEXAFS spectra of the material resulting in thickness maps with step size of 19 nm. Procedure to model the core-shell structure of the NP and obtain core and shell compositions is given in ESI.

Film deposition

The excess of surfactant was removed by dialysis using centrifugation dialysis tubes purchased from Sartorius (Vivaspin 30 kDa MWCO – 20mL). Several dialysis steps were performed by centrifugation at 5000 rpm for 5 min until the conductivity of the filtrate was less than 10 µS/cm.

For all devices, films of NPs were then deposited by spin-coating a 17.5 mg/mL NPs dispersion onto the corresponding substrate, using the following program: spinning speed of 1000 rpm and acceleration 100 rpm/s during 60 s. 1, 2 or 3 layers were deposited, with drying under vacuum at 20°C during 3 hours between each layer. The thickness of the films was measured using a Dektak 150 stylus surface profiler.

Grazing-Incidence Wide-Angle X-ray Scattering GIWAXS:

GIWAXS at Pohang Accelerator Laboratory: GIWAXS measurements were conducted at PLS-II 9A U-SAXS beamline of Pohang Accelerator Laboratory (PAL) in Korea, and at SIRIUS beamline of SOLEIL synchrotron (Saclay, France). Samples consisted in thin-films deposited on silicon wafer (thickness was less than 50 nm). The detailed measurement procedures can be found in the ESI.

Space-charge-limited current (SCLC) devices

Hole-only and electron-only diodes were elaborated to extract the charge-carrier mobility in SCLC device. Hole-only diodes had a Glass:ITO/ZnO/NPs/Ca:Al structure while electron-only diodes had a

Glass:ITO/PEDOT:PSS/NPs/MoO_3:Ag structure. The complete elaboration procedure is described in ESI. The SCLC regime was assessed by using several active-layer (NPs) thicknesses and the charge-carrier mobility was extracted using the Mott-Gurney variation of the current-density versus voltage in the space-charge limited regime.

Organic field-effect transistor OFET

Bottom contact bottom gate organic field-effect transistors (OFETs) were elaborated on commercially available pre-patterned test structures. The detailed elaboration procedure can be found in ESI. One layer of dialysed NPs suspensions at 17.5 $mg.mL^{-1}$ was used as the OFET channel. The charge carrier mobility was extracted in the saturation regime using the usual formalism on transfer characteristics.

Organic photovoltaic (OPV) cells

The OPV device elaboration procedure is described in the supporting informations. The OPV cell structure was Glass:ITO/ZnO/NPs/MoO_3:Ag. The photovoltaic parameters were extracted from current-density versus voltage characteristics measured under a standard AM1.5G (100 mW/cm^2) illumination provided by a calibrated Sun 3000 solar simulator (LOT-Oriel). Spectral response was measured inside a nitrogen-filled glovebox using a home-made setup described in ESI.

Results and discussion

Synthesis of the NP and characterization

Composites NPs containing both materials, the electron donor PF2 and the electron acceptor $PC_{71}BM$, were prepared by miniemulsion, starting from a solution of the materials in chloroform with total concentration of 1 $mg.mL^{-1}$ and variable (D:A) ratios of (10:0), (8:2), (6:4), (5:5), (4:6), (2:8) and (0:10). The solution was emulsified in a sodium dodecylsulfate (SDS) aqueous solution at 4 $mg.mL^{-1}$ under sonication, prior to evaporation of the chloroform, leading to solid composite NPs of (60 ± 30) nm as measured by Dynamic Light Scattering (DLS). No significant size variation of the NPs was observed with the variation of (D:A) ratio. However, it was possible to tune the diameter of the NPs by changing the SDS concentration as shown in **Fig. 1b**. Indeed, the diameter of (PF2:$PC_{71}BM$) composite nanoparticles decreases from (200 ± 70) nm to (60 ± 20) nm when the SDS concentration increases from 0.1 $mg.mL^{-1}$ to 4 $mg.mL^{-1}$. Above 4 $mg.mL^{-1}$, the diameter of (PF2:$PC_{71}BM$) composite NPs reaches a plateau at (60 ± 30) nm, probably because the sonication is not strong enough to break the droplet of the emulsion into smaller droplets.

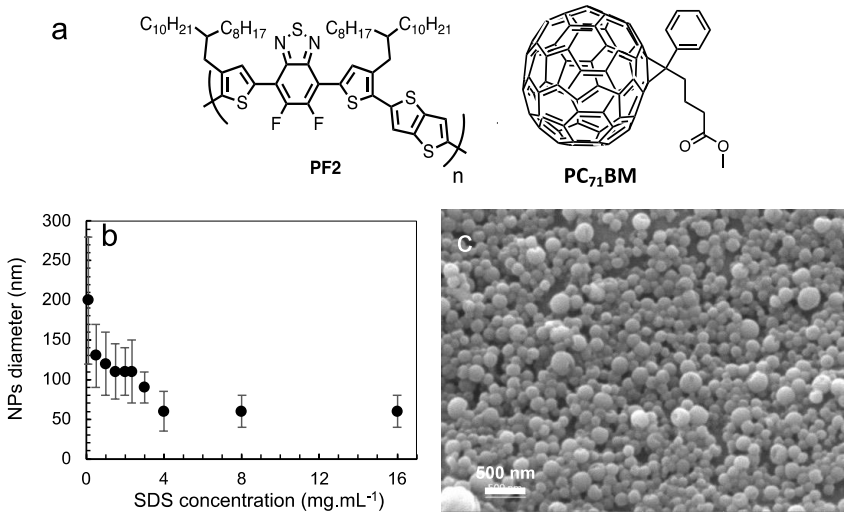

Fig. 1: *a) Molecular structures of PF2 and $PC_{71}BM$, b) Effect of SDS concentration on NPs composites (PF2: $PC_{71}BM$) (4:6), c) SEM image of 200nm NPs with (PF2:$PC_{71}BM$) ratio (4:6).*

SEM image of the NPs shows the spherical morphology and smooth surface of (PF2:$PC_{71}BM$) composite NPs (**Fig. 1c**). However, a deeper morphological characterization is required in order to confirm the presence of the donor and acceptor in the same particles and to determine their distribution within the NPs, which will impact the morphology of the final active layer thin-films used in optoelectronic devices.

First, steady state fluorescence spectroscopy was used to confirm the presence of electron-donor and electron-acceptor components close to each other in the same particles. **Fig. 2a** shows the fluorescence spectra obtained by excitation at 630 nm, for (PF2:$PC_{71}BM$) composite NPs dispersions with different ratio from (10:0) to (0:10). Only PF2 absorbs the light at 630 nm and fluoresces. PF2 fluorescence is almost quenched for every ratio (PF2:$PC_{71}BM$) except when there is no $PC_{71}BM$ (10:0) and fluorescence quenching is a direct signature of an electron transfer from PF2 to $PC_{71}BM$ taking place at the interface between the donor and the acceptor.[18] This electron transfer occurring over length scale of few to tens of nanometers, it is obvious that PF2 and $PC_{71}BM$ are located in the same particle. To further support this statement, fluorescence spectroscopy was performed with mixed separate PF2 and $PC_{71}BM$ NPs (**Fig. 2b**). PF2 and $PC_{71}BM$ are then not enclosed in the same particles and the fluorescence decreases proportionally to PF2 NPs concentration, the total concentration remaining constant. Once again, only PF2 absorbs the light at 630 nm and fluoresces meaning that when PF2 NPs are replaced by an equivalent amount of $PC_{71}BM$ NPs, the fluorescence decreases but is not quenched meaning that charge transfer does not happen as the two materials are too far away in distinct NPs.

Then, time resolved photoluminescence spectroscopy was performed in order to estimate the exciton lifetime. Exciton lifetime decreases when a charge transfer occurs from the donor to the acceptor material. Time-resolved PL of pure PF2 NPs and composite (PF2:$PC_{71}BM$) NPs were studied for large

and small particles of diameter of (200 ± 70) nm and (60 ± 20) nm, respectively (**Fig. 2c-d**). The exciton lifetimes were obtained after data curve fitting using a simple exponential (**equation 1)**:

$$PL(t) = PL(t=0)e^{-t/\tau} \qquad (1)$$

where *PL(t)* refers to the PL intensity at time *t*, *PL(t=0)* is the initial photoluminescence signal and $1/\tau$ represents the probability of de-excitation by radiative recombination. For both NPs diameters, the measured τ decreases when the amount of $PC_{71}BM$ increases to reach a value of (0.26 ± 0.05) ns in the case of (PF2:$PC_{71}BM$) composite NPs with a ratio (98.5:1.5) (**Table S3, ESI**). Even with such a low ratio of $PC_{71}BM$ the dissociation of excitons at the donor/acceptor interface is becoming predominant. Adding more $PC_{71}BM$ to the nanoparticles is expected to further decrease the exciton lifetime. Unfortunately, the time resolution of our set-up does not allow us to measure such short time intervals. Therefore, for time-resolved PL experiments, the relative $PC_{71}BM$ ratio was kept below 1.5%.

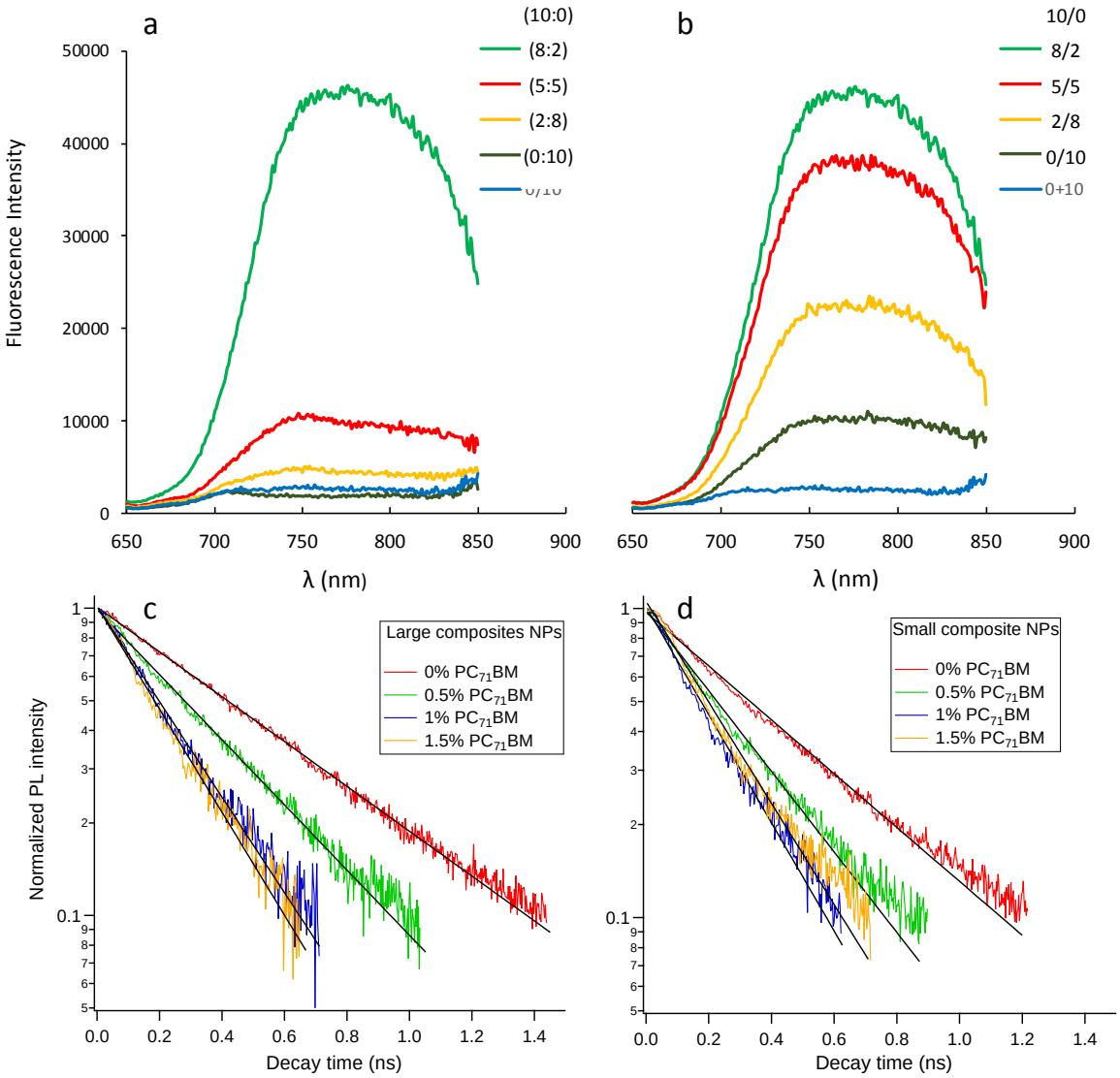

Fig. 2: *Steady state fluorescence spectrum of a) composite (PF2:$PC_{71}BM$) NPs with different weight ratio (wt_{PF2}:wt_{PCBM}), b) mixtures of NPs of pure PF2 with NPs of pure $PC_{71}BM$ with different ratios wt_{PF2}/wt_{PCBM}. Excitation at 630 nm. Suspension concentration used = 0.002 mg.mL^{-1}.*
Normalized PL curve of (c) pure PF2 NPs and (PF2:$PC_{71}BM$) composites NPs with different ratio and a diameter of (200 ± 70) nm (large NPs), (d) pure PF2 NPs and (PF2:$PC_{71}BM$) composites NPs with different ratio and a diameter of (60 ± 20) nm (small NPs). Excitation using a wavelength of 515 nm – pulse duration 90 ps. NPs diameters were measured by DLS.

Morphology of the NPs

The morphology of the NPs was further characterized by using transmission electron microscopy (TEM), confirming the presence of the two components in the particles with a core-shell morphology for large and small NPs (**Fig. 3a,b and Fig. S2)**. However, it was not possible to identify from these images which compound is predominant in the core or in the shell of the nanoparticle. Barr *et al.*,[8] showed in a recent work that the internal structure of organic nanoparticles was controlled by the difference in surface energy of the electron donor polymer and the acceptor material. The material having the lowest surface energy being located in the shell. In PF2 and $PC_{71}BM$ case, the values of their surface energy, measured by tensiometry (ESI) were 30 mN.m^{-1} and 47 mN.m^{-1}, respectively. Moreover, both materials have a very small (<1 mN.m^{-1}) polar component. Therefore, the fluorinated polymer should be preferentially located in the shell while fullerene acceptor occupies the core. In order to confirm the nature and determine the purity of the core and shell domains of the NPs, Scanning Transmission X-Ray Microscopy (STXM) was also performed. This technique allows to map the chemical composition of thin materials, the chemical contrast being obtained thanks to differences in the Near Edge X-ray Absorption Fine Structure (NEXAFS) of the materials given in ESI. However, one should also note that the spatial resolution of the STXM used is of ~30 nm. Therefore, in order to get sufficient insight on the internal morphology of the NPs, only the largest composite NPs could be observed by this technique. Nevertheless, the results obtained on large NPs could be extrapolated to smaller particles exhibiting similar morphology on TEM images ((**Fig. 3a,b and S2**). As observed by TEM, the STXM composition maps show the core-shell structure of the particles (**Fig. 3c,d**) with a $PC_{71}BM$-rich core and a PF2-rich shell as could be predicted from the measured surface energies of the $PC_{71}BM$ (47 mN.m^{-1}) and PF2 (30 mN.m^{-1}).

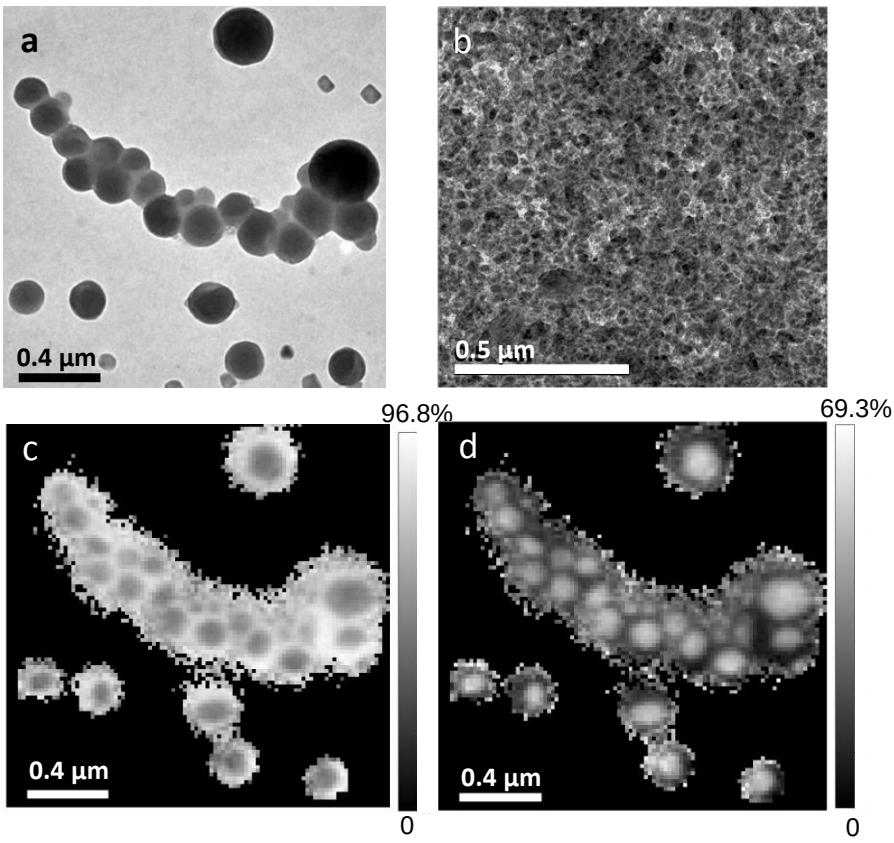

Fig. 3: *(PF2:$PC_{71}BM$) (1:1) nanoparticle without annealing. TEM images of a) large and b) small NPs. c) STXM PF2 composition map and d) STXM $PC_{71}BM$ composition map of large NPs.*

STXM being a transmission method, the composition maps give the composition of the two components for each pixel through the entire particle. The composition profiles of the particles were then measured for each particle and fitted with a core-shell model in order to estimate the relative radius and the real composition of the $PC_{71}BM$-rich core and the PF2-rich shell. The analysis is described in **ESI** and results obtained from analysis of around 10 particles per sample are given in **Table 1**. The measurements were performed for dialyzed suspension of (PF2:$PC_{71}BM$) (1:1) composite nanoparticle without annealing (**Fig. 3**) or after thermal annealing for 10 min at 150°C (**Fig. S7**).

Table 1: *Results obtained from the fit of the particles profile using a core-shell particle model. Relative core radius is the ratio of the core radius to the total radius of the particle.*

	Relative core radius	**PF2 in core (wt%)**	**PF2 in shell (wt%)**
NPs before annealing	0.59 ± 0.07	33 ± 11	75 ± 7
NPs annealed at 150°C / 10 min	0.54 ± 0.17	35 ± 11	58 ± 8

Before annealing, NPs have a $PC_{71}BM$-rich core containing around 70 wt% of $PC_{71}BM$ and 30 wt% of PF2, and a PF2-rich shell with around 75 wt% of PF2 and 25 wt% of $PC_{71}BM$. A significant difference was observed for the composition of the PF2-shell after annealing at 150°C during 10 min. $PC_{71}BM$ content within the shell increases from 25 wt% initially to 42 wt%. This value is much higher than the percolation threshold of PCBM for electron mobility observed by Vakhshouri *et al.*[19] in binary mixtures of amorphous polymers. During annealing, the diffusion of $PC_{71}BM$ through the shell should thus allow an increase of the percolation paths for the electrons transport towards the electrodes.

Thin films preparation and characterization

The suspensions of synthetized composite nanoparticles ((PF2:$PC_{71}BM$) (1:2), (60 ± 20) nm in diameter) were dialysed to remove SDS and concentrated at 17.5 $mg.mL^{-1}$ prior to deposition by spin-coating.

Despite the numerous centrifugal dialysis steps (up to 16 successive steps), an estimated minimum of 20 wt% SDS, corresponding approximately to a SDS monolayer adsorbed on the nanoparticle surface, is still present in the NPs suspension as shown by ATG measurement (ESI).

Thin films with thicknesses ranging from (70 ± 10) nm to (200 ± 10) nm were obtained by spin-coating deposition of 1 to 3 NP layers (1 to 3 spin-coating deposition steps). Thermal annealing at different temperatures was then performed in order to compact the film, and allow partial coalescence of the NP. After spin-coating, the film roughness is in the order of 20 nm. When annealed for 10 min at 120°C, AFM reveals a decrease in film roughness to 10 nm, as well as coalescence of the NPs in the film. However, annealing for 10 min at 160°C leads to visible phase separation in AFM, together with an increase in roughness to 100 nm (**Fig. 4**). This difference in final morphology illustrates the importance of thermal annealing, after deposition, in order to optimize active layer properties.

Grazing incidence wide angle X-ray scattering (GIWAXS) was used to characterize the structure and morphology of the donor PF2 and the acceptor $PC_{71}BM$ materials within the thin films as a function of the annealing temperature. As shown in **Fig. 5**, in the absence of annealing or for annealing below 150°C, patterns are undistinguishable from juxtaposition of neat PF2 and $PC_{71}BM$ domains, as can be seen for pure PF2 NPs and pure $PC_{71}BM$ NPs (**Fig. S11-13**). Indeed **Fig. 5a-c** shows a series of lamellar reflection (*h*00) corresponding to a mesomorphous solid state M_{Lam} characteristic to the lamellar structure of PF2 and the scattering rings of the amorphous $PC_{71}BM$ phase.[13] The film annealed at 150°C maintains an equivalent lamellar periodicity but the appearance of numerous reflections reveals the crossing of a phase transformation (**Fig. 5d**). Besides the (*h*00) spots that acquire a dot-like shape, other (*hkl*) spot series extending to high *h* are now visible (green arrows), which indicates well-defined crystalline lamellae that are well-oriented parallel to the substrate. Therefore, the stacking directions of polymer backbones and main conduction pathways essentially lie in the film plane. Note the new reflections appearing in the small-angle region (green stars), which

implies a large lattice structure or possibly phase coexistence. Otherwise, scattering rings of amorphous $PC_{71}BM$ have vanished and are not replaced by the reflections of crystalline $PC_{71}BM$ (**Fig. S13**). This suggests that a mixed structure incorporating $PC_{71}BM$ in PF2 lamellae has been formed. As a conclusion, a phase change that could be related to a co-crystallization of both materials has been seen starting from 150°C, also visible on the AFM image after curing at 160°C (**Fig. 4c**).

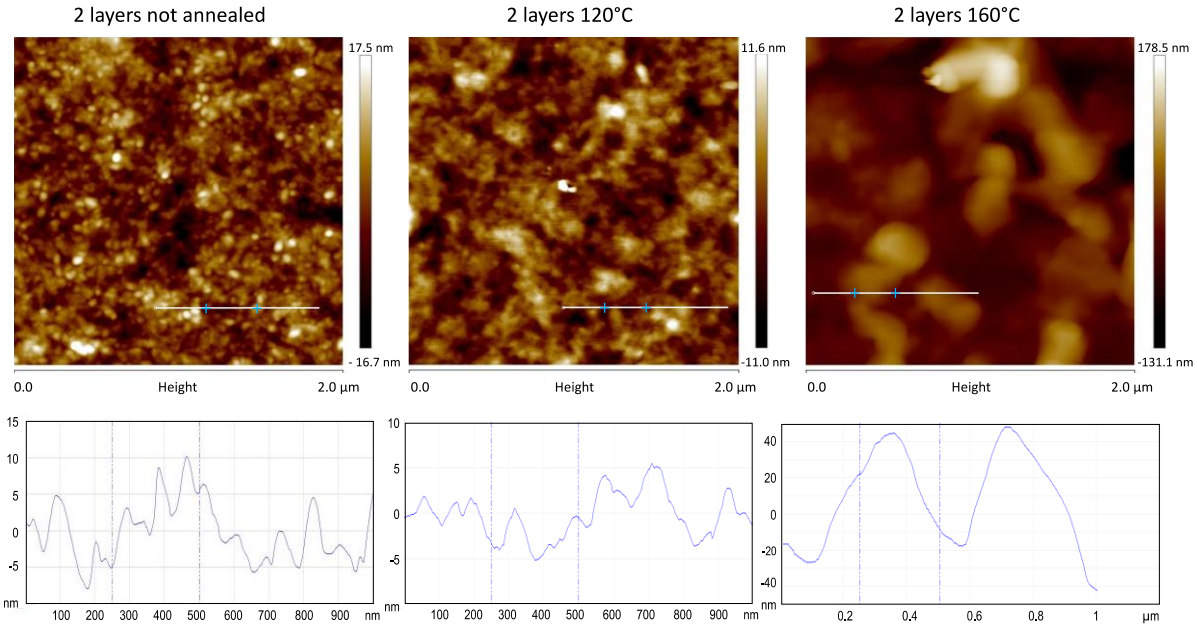

Fig. 4: *AFM height images (2µm x 2µm) and roughness profiles of 2-layers thin films of NPs deposited by spin-coating, with or without thermal annealing. Mean film thickness of 140 nm (left not annealed – middle 120°C - right 160°C)*

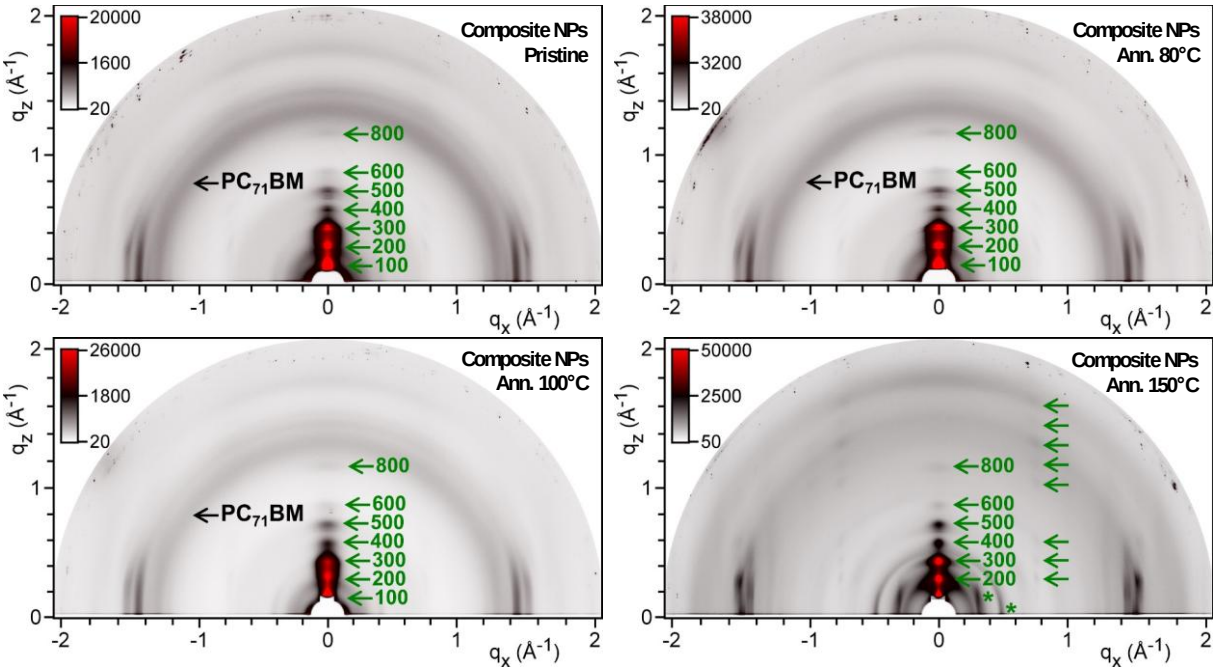

Fig. 5: *GIWAXS patterns of a (PF2:$PC_{71}BM$) composite NP film, as prepared and after annealing at different temperatures.*

Charge transport in NPs films and OPV measurements

Charge carrier mobilities are known to be highly sensitive to the thin-film morphology i.e. volume distribution of D and A materials, orientations of π-stacked lamellas with respect to the substrate. The perpendicular charge carrier mobilities of composite (PF2:PCBM) (1:2) NPs-based thin films has been investigated through space charge limited current (SCLC) devices elaboration and characterization. Organic field-effect transistors (OFETs) have been also used to probe the in-plane hole mobility. In both cases, the focus was on the evolution of charge transport properties as a function of thermal annealing. Holes mobilities have been measured in both devices, but in contrast, electrons mobilities were only studied by SCLC. Indeed, in bottom gate/bottom contacts OFETs, due to the presence of hydroxyl groups on the surface of the SiO_2 that could act as electron traps, the SiO_2 surface is usually functionalized by HMDS or OTS monolayers to get rid of these hydroxyl groups. Unfortunately, such surface treatments render the substrate highly hydrophobic leading to dewetting of the aqueous NPs suspensions and consequently cannot be applied for water-suspended NPs deposition.

The SCLC mobilities have been extracted for several active-layer thicknesses as a function of annealing temperature. For instance, on 140 nm thick films prepared from (PF2:$PC_{71}BM$) (1:2) composite NPs, the electron mobility (μ_{e-}) increases slightly from $(5 \pm 2)x10^{-3}$ $cm^2/(V.s)$ for as-cast samples up to $(6 \pm 2)x10^{-3}$ $cm^2/(V.s)$ and $(7.5 \pm 3)x10^{-3}$ $cm^2/(V.s)$ after an isochronal (10 min.) annealing at a temperature of 100°C and 120°C, respectively. This result shown in **Fig. 6a** agrees with a possible core-shell NPs melting, allowing a slight $PC_{71}BM$ diffusion and may also be related to partial NPs coalescence, as observed by AFM. At higher annealing temperature, 140°C and 160°C, a drop of the electron mobility occurred ($\mu_{e-} = (2 \pm 1.5)x10^{-3}$ $cm^2/(V.s)$). Although the high-temperature morphology is not fully understood, electron mobility measurements, combined with AFM and GIWAXS measurements, confirm the idea of phase change around 140-150°C, with possible crystallization or co-crystallization of the materials.

Similar to the electron mobility, annealing has a huge impact on the hole mobility (μ_{h+}) related to the donor material PF2. The μ_{h+} extracted from SCLC devices, decreases when applying a thermal annealing to the substrate (**Fig. 6b**). Indeed, the hole mobility decreases from $(1.3 \pm 0.4)x10^{-3}$ $cm^2/(V.s)$ for non-annealed substrate to $(0.5 \pm 0.4)x10^{-3}$ $cm^2/(V.s)$, when the SCLC device has undergone a thermal annealing at 140°C for 10 minutes. Inversely, the hole mobility measured by OFET increased when the substrates were thermally annealed. The OFET hole mobility increases when the annealing temperature increases to achieve a value of $(2.6 \pm 0.4)x10^{-4}$ $cm^2/(V.s)$ after thermal annealing at 160°C (10 min.) compared to a weak OFET μ_{h+} of $(6.7 \pm 0.8)x10^{-7}$ $cm^2/(V.s)$ for non-annealed substrates.

This contradictory behavior of thermal annealing effect on holes mobility, as measured by SCLC and OFET devices, can certainly be related to the orientation of the PF2 molecules after thermal annealing as reported in the GIWAXS analyses. Before thermal annealing, PF2 molecules have a mixed, balanced face-on and edge-on orientation with respect to the electrodes, while after annealing at 150°C, the proportion of PF2 edge-on orientation increases involving preferential charge transport in the direction parallel to the substrates. Consistently, the SCLC hole-mobility is divided by two after thermal annealing at 140°C (around $5x10^{-4}$ $cm^2/(V.s)$) while the OFET hole mobility is multiplied by almost 150 (around $1x10^{-4}$ $cm^2/(V.s)$).

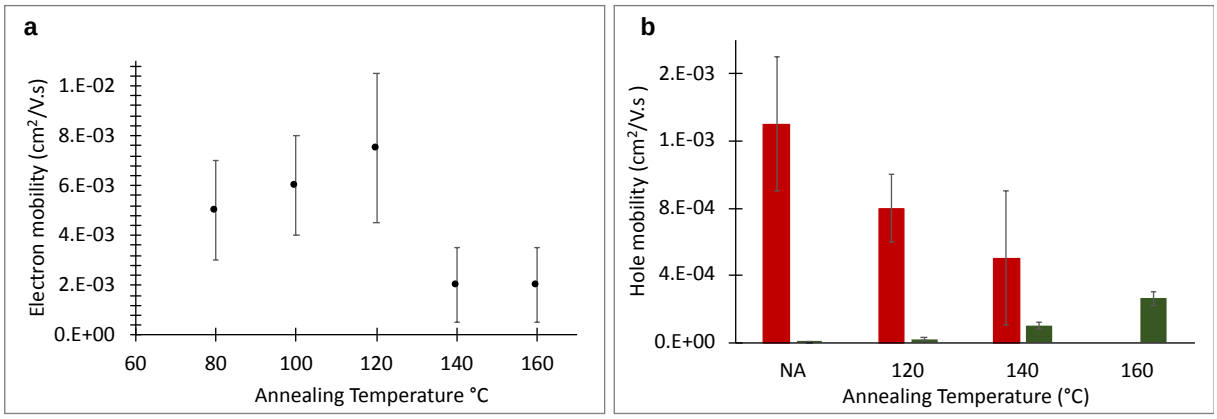

Fig. 6: *Charge carrier mobilities measured for composite (PF2:$PC_{71}BM$) (1:2) NPs thin films as a function of annealing temperature (NP diameters = (60 ± 20) nm). a) Electron mobility measured by SCLC on 140 nm-thick films, b) hole mobility measured by SCLC on 140 nm-thick films (red), and by OFET (green). Each thermal annealing step duration is 10 minutes.*

Several devices were elaborated to test the photovoltaic properties of the composite NPs (1:2) solar cells. The active layer thickness was varied by sequential deposition of one, two or three NPs layers (see ESI for details) and 10 min. Thermal annealing steps at various temperatures were applied to the device before the top-electrode deposition. It should be noted that thermal annealing after top-electrode deposition was always detrimental to photovoltaic performances. The best photovoltaic results were obtained on two layers deposited NPs devices annealed at 120°C for 10 minutes before top-electrode deposition. The current density (*J*) versus voltage (*V*) of the best diode in the dark at under standard AM1.5G (100 mW/cm^2) illumination can be found in **Fig. 7a**. The photovoltaic parameters of this diode are displayed in **Table 2** together with the ones measured on a bulk heterojunction (BHJ) solar cell elaborated with the same electron donor (PF2) and acceptor ($PC_{71}BM$) materials with a weight ratio (1:1.5). This BHJ device was made by applying the optimized conditions reported in Ibraikulov *et al*. for the PF2/$PC_{71}BM$ blend.[13]

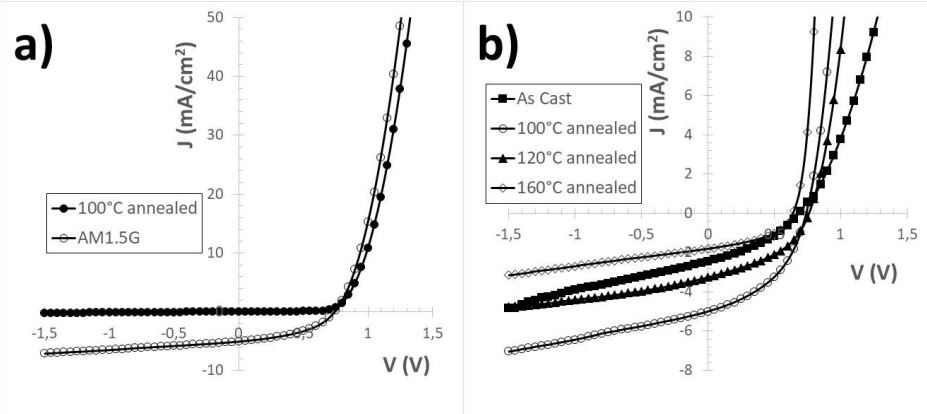

Fig. 7: *a) (J-V) characteristics of the best NPs OPV cell in the dark (closed circles) and under standard AM1.5G (100 mW/cm^2) illumination (open circles). b) (J-V) characteristics under standard AM1.5G (100 mW/cm^2) of NPs OPV cells elaborated with two layers of composite (PF2:PC$_{71}$BM) (1:2) NPs. OPV cells were not annealed (closed squares) or annealed for 10 minutes at 100°C (open circles), 120°C (closed triangles) and 160°C (open diamonds), respectively.*

Table 2: *Photovoltaic parameters of a bulk heterojunction OPV cells prepared from (PF2:PCBM) solution in o-DCB (1:1.5) and from the best (PF2:PC$_{71}$BM) (1:2) composite NPs in water. The active layer thickness was measured by profilometry, The OPV area was 12 mm^2.*

Conditions	V_{OC} (mV)	J_{SC} (mA.cm^{-2})	FF (%)	Thickness of the active layer (nm)	PCE (%)
BHJ solution no annealing	760	17.8	66	235	9
NPs – 100°C	749	5.0	43	140	1.6

On the one hand, as can be seen in **Table 2**, the open-circuit voltage (V_{oc}) is in the same range for the BHJ and the NPs devices. On the other hand, the fill factor (*FF*) as well as the short-circuit current-density (J_{sc}) are much lower when using a NPs active-layer. We could think that the low J_{sc} measured in the NPs device is due to the lower active-layer thickness (140 nm compared to 235 nm) of the NPs device. This is not the case as increasing the active-layer thickness from one layer of NPs (70 nm) to two layers of NPs (140 nm) has no significant impact on J_{sc}. Moreover, the very weak *FF* is in-line with charge-extraction limitations in the case of the NPs active-layer. Despite charge extraction limitations, a best power conversion efficiency of 1.6% was obtained for this annealed two NPs layer OPV cell.

The effect of a thermal annealing before top-electrode deposition was tested on two NPs layer OPV cells as shown in **Fig. 7b** and **Table 3**.

Table 3: *Photovoltaic parameters of (PF2:PC$_{71}$BM) (1:2) composite NPs in water with or without thermal annealing (10 minutes) before the top-cathode deposition.*

Annealing conditions	V_{OC} (mV)	J_{SC} (mA.cm^{-2})	FF (%)	PCE (%)
no annealing	710	2.4	36	0.6
100°C	749	5.0	43	1.6
120°C	765	3.2	42	1.0
160°C	650	1.8	45	0.5

An annealing step at 100°C prior to top-electrode deposition is obviously necessary to increase V_{oc} (+ 5%) and even more importantly J_{sc} (+ 108%) and *FF* (+ 19%). This increase is in-line with a partial diffusion of $PC_{71}BM$ from the core to the shell of the NPs, favoring percolation pathways for electrons and charge extraction. Annealing at 120°C increases again slightly the open-circuit voltage (+ 2%) but strongly decreases J_{sc} (- 36%). With an almost unchanged *FF*, the power conversion efficiency decreases substantially (- 37%). Finally, a 160°C annealing strongly affects all the parameters except *FF*.

In order to further understand the evolution of the photovoltaic parameters and to highlight the dominant charge-carrier dynamic parameter responsible for the modest PCE measured, we performed photovoltaic measurements as a function of the incident light intensity, keeping the illumination spectrum constant (ESI). The variation of V_{oc} as a function of the light intensity indicates that, for high illumination intensities (above 10 mW/cm^2), bimolecular recombination as well as trap-assisted carrier recombination occur. Moreover, at low light intensities (below 10 mW/cm^2), trap-assisted charge-carrier recombination dominates. It is reasonable to assume that the charge-carrier extraction to the electrodes is a problem in these devices, even after thermal annealing favoring percolation paths for electrons, and that the NPs surface may act as a very efficient charge-carrier trap at annealing temperatures around 100°C. Finally, the spectral response of 2 layers NPs-based devices annealed at 100°C prior to electrode deposition was measured and compared to a BHJ solar cell one with the same donor and acceptor materials. The BHJ PV cell used is the same as the one in **Table 2**. The spectral response for the BHJ and the NPs solar cells can be found in **Fig. 8a**.

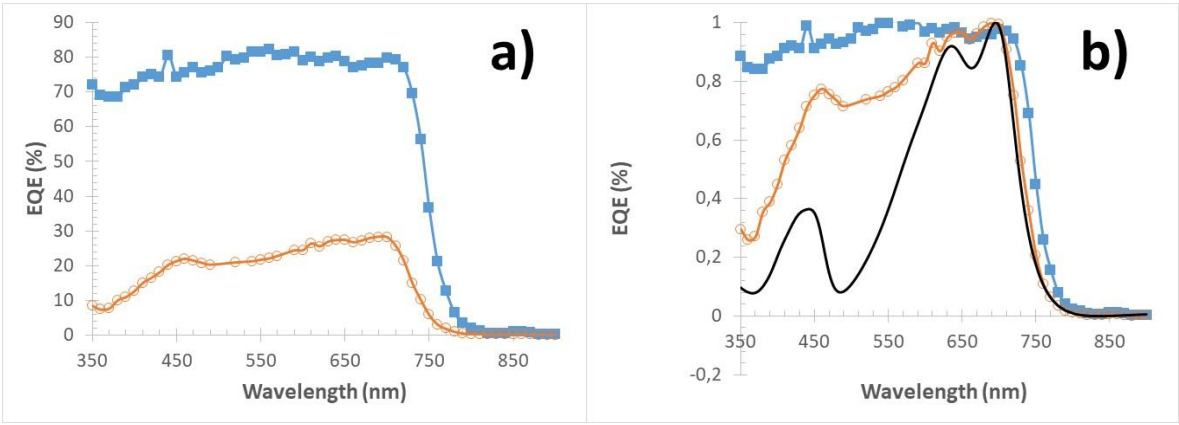

Fig. 8: *a) Spectral response of a BHJ (PF2:$PC_{71}BM$) (1:1.5) solar cell (closed squares) and of a composite NPs (PF2:$PC_{71}BM$) (1:2) solar cell (open circles). b) Same normalized spectral responses as in a) together with the normalized absorption spectrum of PF2 in thin-film (plain black line).*

The External Quantum Efficiency (EQE) is rather flat for the BHJ solar cell (PF2:$PC_{71}BM$) (1:1.5) with values ranging from 70% to 80% in the 300 to 760 nm wavelength range. The EQE for the NPs composite (PF2:$PC_{71}BM$) (1:2) is much weaker over the same spectral range (from 10% to 30%) as expected from the much lower J_{sc}. More interestingly, when looking at the normalized spectra (**Fig. 8b**), the NPs composite solar cell EQE is especially weak in the 350 to 500 nm wavelength range. This wavelength range corresponds to the region were PF2 is less absorbing and $PC_{71}BM$ absorption is maximized. This is evidenced by the superposition of the normalized thin-film PF2 absorption spectrum also present in **Fig. 8b**. Even with proportionally more $PC_{71}BM$ in NPs than in BHJ solar cells, charge generation and extraction from $PC_{71}BM$ seems problematic in NPs solar cells. It means that, even if $PC_{71}BM$ diffuses from the core to the shell upon thermal annealing in NPs solar cells, exciton dissociation or/and electron transport to the electrodes are two major bottlenecks for these systems.

Conclusion

In this article, we demonstrate that organic optoelectronic devices can be fabricated from NPs in aqueous suspension obtained by miniemulsion. We show that it is possible to finely elucidate the internal structure of the mixed nanoparticles by using STXM. In particular, the internal morphology of the initial core-shell NPs is significantly modified upon thermal annealing through a $PC_{71}BM$ percolation from the core towards the shell. Such a $PC_{71}BM$ percolation positively affects the electron transport properties in NPs thermally annealed thin films. In addition, thermal annealing is responsible of NPs coalescence, which is also required to reach suitable charge transport properties. Thanks to GIWAXS, this study also highlights that a compromise must be found in the temperatures used, since the orientation of the polymer chains, relative to the surface, changes with thermal annealing. In the

case of mixed NPs of PF2 and $PC_{71}BM$, an annealing temperature above 100°C, although positive for electron mobility (better $PC_{71}BM$ percolation), reduces the conversion efficiency of the solar cells because of the edge-on reorientation of the polymers, which decreases the hole mobility. Despite relatively low power conversion efficiencies measured during this study (1.6%), the deep understanding of the relationships between the NPs structural evolution and their optoelectronic properties is essential to improve the NPs organic photovoltaic devices performances. In addition, such mixed OSCs NPs have recently found applications in photocatalysis, in particular for the production of solar fuels. Therefore, the study of the NPs elaboration and their structural and optoelectronic properties is essential and needs to be intensified in order to limit our dependence toward fossil fuels.

Conflicts of Interest

There are no conflicts of interest to declare.

Acknowledgements

This study was supported by the Agence Nationale de la Recherche, France (project ANR-17-CE09-0012 FORCE). We acknowledge SOLEIL synchrotron for the STXM measurements performed at the HERMES beamline (project 20193019) as well as GIWAXS measurements at SIRIUS beamline with the assistance of Dr Arnaud Hemmerle for adjustments.

We thank Christophe Contal (ICS) for AFM images and the TEM plateform of IPCMS for TEM analyses.

Finally, we also acknowledge Pohang Accelerator Laboratory (PAL) for giving us the opportunity to perform the GIWAXS measurements, MEST and POSTECH for supporting these experiments, Dr Hyungju Ahn for adjustments and help, and other colleagues from the 9A USAXS beamline for assistance.

Bibliography

1 Y. Cui, Y. Xu, H. Yao, P. Bi, L. Hong, J. Zhang, Y. Zu, T. Zhang, J. Qin, J. Ren, Z. Chen, C. He, X. Hao, Z. Wei and J. Hou, Single-Junction Organic Photovoltaic Cell with 19% Efficiency, *Adv. Mater.*, 2021, **33**, 2102420.

2 B. Mohamed El Amine, Y. Zhou, H. Li, Q. Wang, J. Xi and C. Zhao, Latest Updates of Single-Junction Organic Solar Cells up to 20% Efficiency, *Energies*, 2023, **16**, 3895.

3 S. Lee, D. Jeong, C. Kim, C. Lee, H. Kang, H. Y. Woo and B. J. Kim, Eco-Friendly Polymer Solar Cells: Advances in Green-Solvent Processing and Material Design, *ACS Nano*, 2020, **14**, 14493–14527.

4 J. Wang, I. Rodriguez-Donis, S. Thiebaud-Roux, O. A. Ibraikulov, N. Leclerc, P. Lévêque, V.

Gerbaud, M. Kohlstädt and T. Heiser, Selection of green solvents for organic photovoltaics by reverse engineering, *Mol. Syst. Des. Eng.*, 2022, **7**, 182–195.
5 M. Rammal, P. Lévêque, G. Schlatter, N. Leclerc and A. Hébraud, Recent advances in the green elaboration of organic photovoltaic devices from nanoparticle dispersions, *Mater. Chem. Front.*, 2020, **4**, 2904.
6 M. Marks, N. P. Holmes, A. Sharma, X. Pan, R. Chowdhury, M. G. Barr, C. Fenn, M. J. Griffith, K. Feron, A. L. D. Kilcoyne, D. A. Lewis, M. R. Andersson, W. J. Belcher and P. C. Dastoor, Building intermixed donor–acceptor architectures for water-processable organic photovoltaics, *Phys. Chem. Chem. Phys.*, 2019, **21**, 5705–5715.
7 S. Subianto, R. Balu, L. de Campo, A. Sokolova, N. K. Dutta and N. R. Choudhury, Sulfonated Thiophene Derivative Stabilized Aqueous Poly(3-hexylthiophene):Phenyl-C61-butyric Acid Methyl Ester Nanoparticle Dispersion for Organic Solar Cell Applications, *ACS Appl. Mater. Interfaces*, 2018, **10**, 44116–44125.
8 M. G. Barr, S. Chambon, A. Fahy, T. W. Jones, M. A. Marcus, A. L. D. Kilcoyne, P. C. Dastoor, M. J. Griffith and N. P. Holmes, Nanomorphology of eco-friendly colloidal inks, relating non-fullerene acceptor surface energy to structure formation, *Mater. Chem. Front.*, , DOI:10.1039/D0QM00980F.
9 H. Laval, A. Holmes, M. A. Marcus, B. Watts, G. Bonfante, M. Schmutz, E. Deniau, R. Szymanski, C. Lartigau-Dagron, X. Xu, J. M. Cairney, K. Hirakawa, F. Awai, T. Kubo, G. Wantz, A. Bousquet, N. P. Holmes and S. Chambon, Toward High Efficiency Water Processed Organic Photovoltaics: Controlling the Nanoparticle Morphology with Surface Energies, *Adv. Energy Mater.*, 2023, 2300249.
10 D. Horn and J. Rieger, Organic nanoparticles in the aqueous phase—theory, experiment, and use, *Angew. Chem. Int. Ed.*, 2001, **40**, 4330–4361.
11 E. Lepeltier, C. Bourgaux and P. Couvreur, Nanoprecipitation and the “Ouzo effect”: Application to drug delivery devices, *Adv. Drug Deliv. Rev.*, 2014, **71**, 86–97.
12 S. Gärtner, A. J. Clulow, I. A. Howard, E. P. Gilbert, P. L. Burn, I. R. Gentle and A. Colsmann, Relating Structure to Efficiency in Surfactant-Free Polymer/Fullerene Nanoparticle-Based Organic Solar Cells, *ACS Appl. Mater. Interfaces*, 2017, **9**, 42986–42995.
13 O. A. Ibraikulov, C. Ngov, P. Chávez, I. Bulut, B. Heinrich, O. Boyron, K. L. Gerasimov, D. A. Ivanov, S. Swaraj, S. Méry, N. Leclerc, P. Lévêque and T. Heiser, Face-on orientation of fluorinated polymers conveyed by long alkyl chains: a prerequisite for high photovoltaic performances, *J. Mater. Chem. A*, 2018, **6**, 12038–12045.
14 X. Ma, Q. An, O. A. Ibraikulov, P. Lévêque, T. Heiser, N. Leclerc, X. Zhang and F. Zhang, Efficient ternary organic photovoltaics with two polymer donors by minimizing energy loss, *J. Mater. Chem. A*, 2020, **8**, 1265–1272.
15 Olzhas. A. Ibraikulov, J. Wang, N. Kamatham, B. Heinrich, S. Méry, M. Kohlstädt, U. Würfel, S. Ferry, N. Leclerc, T. Heiser and P. Lévêque, ITO-Free Organic Photovoltaic Modules Based on Fluorinated Polymers Deposited from Non-Halogenated Solution: A Major Step Toward Large-Scale Module Production, *Sol. RRL*, 2019, **3**, 1900273.
16 R. Belkhou, S. Stanescu, S. Swaraj, A. Besson, M. Ledoux, M. Hajlaoui and D. Dalle, HERMES: a soft X-ray beamline dedicated to X-ray microscopy, *J. Synchrotron Radiat.*, 2015, **22**, 968–979.
17 Y. Ma, C. T. Chen, G. Meigs, K. Randall and F. Sette, High-resolution K-shell photoabsorption measurements of simple molecules, *Phys. Rev. A*, 1991, **44**, 1848–1858.
18 S. N. Clafton, D. M. Huang, W. R. Massey and T. W. Kee, Femtosecond Dynamics of Excitons and Hole-Polarons in Composite P3HT/PCBM Nanoparticles, *J. Phys. Chem. B*, 2013, **117**, 4626–4633.
19 K. Vakhshouri, D. R. Kozub, C. Wang, A. Salleo and E. D. Gomez, Effect of Miscibility and Percolation on Electron Transport in Amorphous Poly(3-Hexylthiophene)/Phenyl-${\mathrm{C}}_{61}$-Butyric Acid Methyl Ester Blends, *Phys. Rev. Lett.*, 2012, **108**, 026601.